

# Investigation of the Reversible Intercalation/Deintercalation of Al into the Novel $\text{Li}_3\text{VO}_4@\text{C}$ Microsphere Composite Cathode Material for Aluminum-Ion Batteries

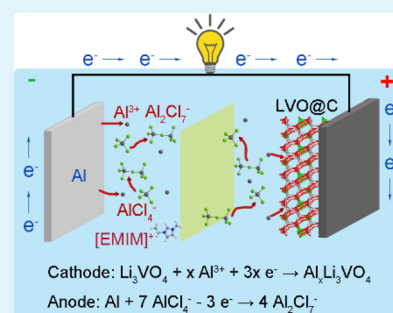
Jiali Jiang, He Li,<sup>1</sup> Jianxing Huang, Kun Li, Jing Zeng, Yang Yang, Jiaqi Li, Yunhui Wang, Jing Wang, and Jinbao Zhao\*<sup>1</sup>

State Key Laboratory of Physical Chemistry of Solid Surfaces, Collaborative Innovation Center of Chemistry for Energy Materials, State-Province Joint Engineering Laboratory of Power Source Technology for New Energy Vehicle, College of Chemistry and Chemical Engineering, Xiamen University, No. 422 Siming South Road, Xiamen, Fujian 361005, China

## Supporting Information

**ABSTRACT:** The  $\text{Li}_3\text{VO}_4@\text{C}$  microsphere composite was first reported as a novel cathode material for rechargeable aluminum-ion batteries (AIBs), which manifests the initial discharge capacity of  $137 \text{ mAh g}^{-1}$  and remains at  $48 \text{ mAh g}^{-1}$  after 100 cycles with almost 100% Coulombic efficiency. The detailed intercalation mechanism of Al into the orthorhombic  $\text{Li}_3\text{VO}_4$  is investigated by ex situ X-ray diffraction (XRD) and X-ray photoelectron spectroscopy (XPS) of  $\text{Li}_3\text{VO}_4@\text{C}$  electrodes and the nuclear magnetic resonance aluminum spectroscopy ( $^{27}\text{Al}$  NMR) of ionic liquid electrolytes in different discharge/charge states. First-principle calculations are also carried out to investigate the structural change as Al inserts into the framework of  $\text{Li}_3\text{VO}_4$ . It is revealed that the  $\text{Al}/\text{Li}_3\text{VO}_4@\text{C}$  battery goes through electrochemical dissolution and deposition of metallic aluminum in the anode, as well as the insertion and deinsertion of  $\text{Al}^{3+}$  cations in the cathode in the meantime. The rechargeable AIBs fabricated in this work are of low cost and high safety, which may make a step forward in the development of novel cathode materials based on the acidic ionic liquid electrolyte system.

**KEYWORDS:** aluminum-ion battery, ionic liquid, cathode,  $\text{Li}_3\text{VO}_4@\text{C}$ , mechanism



## INTRODUCTION

Lithium-ion batteries (LIBs) have been deemed one of the most promising energy conversion and storage systems on account of its high operating voltage, high energy density, and long cycle life.<sup>1</sup> Nevertheless, with the widespread promotion and application of LIBs all over the world in recent decades, lithium resources are faced with the risk of drying up, so the price of lithium metal is rising significantly year by year.<sup>2</sup> However, commercial LIBs usually use carbonates like ethylene carbonate (EC), diethyl carbonate (DEC), and dimethyl carbonate (DMC) as electrolyte solvents, which as flammable and combustible organic solvents will bring potential safety hazards to LIBs.<sup>3–5</sup> Therefore, it is imperative to find a substitute for LIBs to meet the requirements of high safety and large-scale energy storage systems.

Aluminum-ion batteries (AIBs) have recently attracted significant interest because aluminum is the most abundant metallic element and aluminum resources are evenly distributed in Earth's crust.<sup>6–8</sup> In addition, the AIBs with multivalent metal ions transmitting internally can provide a very high capacity ( $2.98 \text{ Ah/g}$  and  $8.05 \text{ Ah/cm}^3$ ).<sup>9</sup> Moreover, ionic liquids as electrolyte of AIBs can greatly improve the safety performance of the battery since its nonflammability and wide electrochemical window.<sup>10</sup> Hence, it is reasonable to conclude that the AIBs will have a great application prospect and value in use for

large-scale smart grid energy storage systems and car batteries that are at risk of collision and explosion.<sup>11</sup> Up to now, the exploration of AIBs is still in early stage. As an important component of the rechargeable AIBs, Al-storage cathode materials have been most lately researched. There are several papers about the Al-ion battery cathode materials reported to date, involving the conversion electrodes such as  $\text{FeS}_2$ <sup>12</sup> and  $\text{Ni}_3\text{S}_2$ <sup>13</sup> and electrodes based on intercalation reactions like graphite materials,<sup>14,15</sup>  $\text{Mo}_6\text{S}_8$ ,<sup>16</sup> and Prussian blue analogues (PBAs).<sup>17,18</sup> Owing to the strong electrostatic repulsion between  $\text{Al}^{3+}$  ions, it should be difficult for aluminum ions to intercalate into the frame structure of active materials.<sup>19</sup> To sum up, a suitable intercalation electrode needs a large enough 2D or 3D framework and wide insertion/extraction channel to accommodate Al embedding back and forth quickly and a material structure which can remain stable in long cycling.<sup>20</sup>

Most recently,  $\text{Li}_3\text{VO}_4$  has been massively reported as a promising anode material for LIBs due to its long cycle life and high reversible capacity.<sup>21,22</sup> The framework of  $\text{Li}_3\text{VO}_4$  can be counted as a hollow lanternlike 3D structure which consists of orderly corner-shared  $\text{VO}_4$  and  $\text{LiO}_4$  tetrahedrons, and there

Received: May 26, 2017

Accepted: August 3, 2017

Published: August 3, 2017

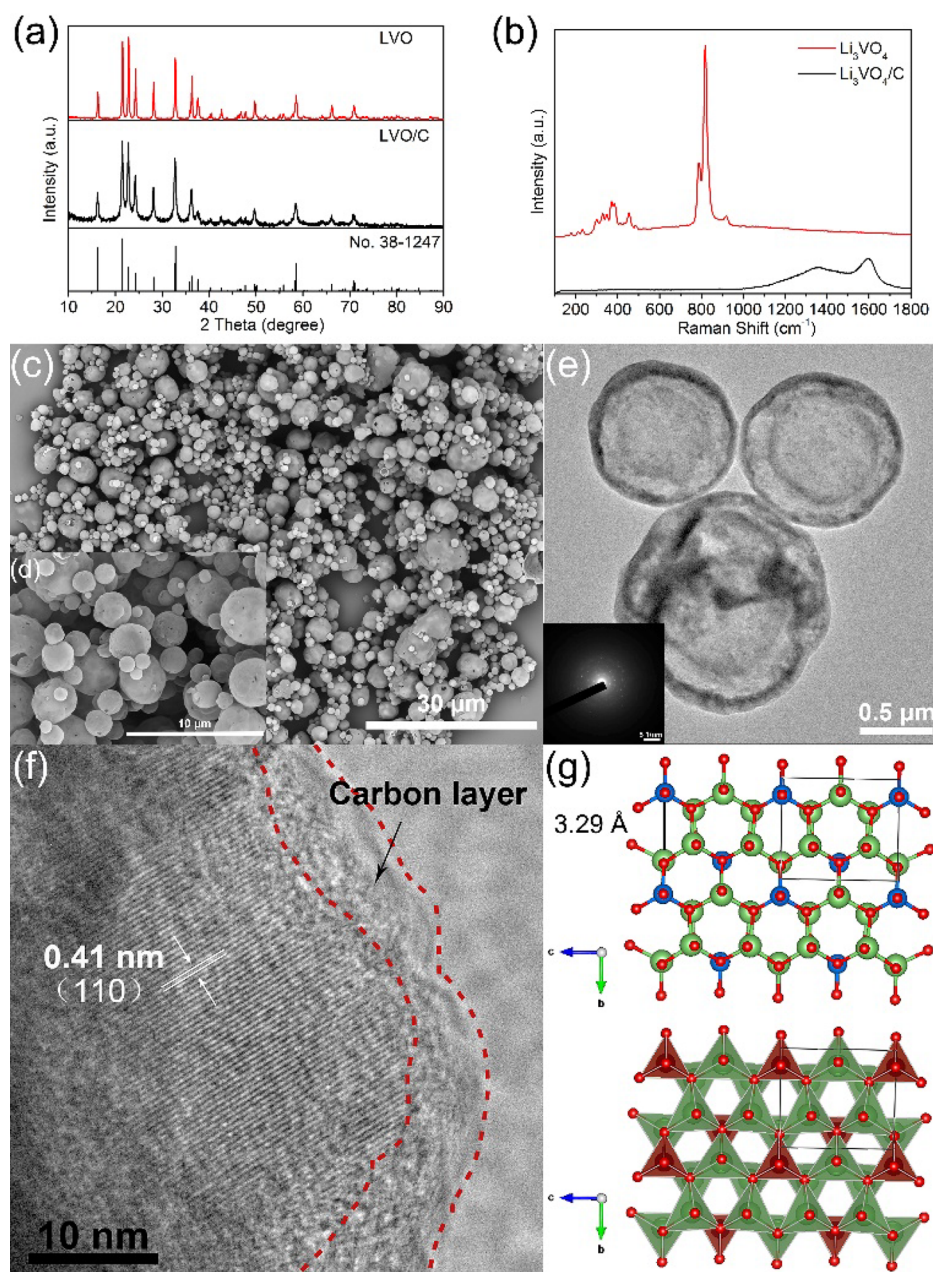


**Figure 1.** (a) XRD patterns and (b) Raman spectra of the as-prepared  $\text{Li}_3\text{VO}_4@\text{C}$  and  $\text{Li}_3\text{VO}_4$ . (c, d) SEM images of  $\text{Li}_3\text{VO}_4@\text{C}$  composite. (e) TEM image and SAED pattern (inset) of  $\text{Li}_3\text{VO}_4@\text{C}$  composite. (f) HR-TEM image of  $\text{Li}_3\text{VO}_4@\text{C}$ . (g) Crystal structure of  $\text{Li}_3\text{VO}_4$  projected along  $a$ -axis. Color code: Li, green; V, dark blue; O, red.

are many empty sites in the hollow lanternlike 3D structure to accommodate ions inserting reversibly,<sup>9</sup> which is shown in Figure 1g. The dynamic diameter of center space is 3.29 Å, much larger than the radius of  $\text{Al}^{3+}$  cations (0.59 Å) but smaller than the size of  $\text{AlCl}_4^-$  (5.28 Å).<sup>13,20</sup> Hence,  $\text{Li}_3\text{VO}_4$  can be a favorable intercalation electrode material for rechargeable AIBs, and predominantly  $\text{Al}^{3+}$  cations insert into the structure of  $\text{Li}_3\text{VO}_4$  upon discharging.

Herein, we report for the first time the fabrication of mesoporous  $\text{Li}_3\text{VO}_4@\text{C}$  hollow spheres composite as a novel cathode material for the rechargeable AIBs. The initial discharge capacity of  $\text{Al}/\text{Li}_3\text{VO}_4@\text{C}$  battery is 137  $\text{mAh g}^{-1}$  and remains at 48  $\text{mAh g}^{-1}$  after 100 cycles with the Coulombic efficiency of near 100%. A pair of redox peaks in cyclic voltammogram show that Al reversibly intercalates/deinterca-

lates into one kind of crystallographic sites of  $\text{Li}_3\text{VO}_4$ , which is also supported by theoretical calculation. Meanwhile, ex situ X-ray diffraction (XRD) and X-ray photoelectron spectroscopy (XPS) of  $\text{Li}_3\text{VO}_4@\text{C}$  electrodes and the nuclear magnetic resonance aluminum spectroscopy ( $^{27}\text{Al}$  NMR) of ionic liquid electrolyte in different states are carried out to evaluate the detailed intercalation mechanism of Al into the orthorhombic  $\text{Li}_3\text{VO}_4$ . It may be reasonable to conclude that the battery undergoes electrochemical deposition and dissolution of metallic aluminum in the anode, as well as the insertion and deinsertion of  $\text{Al}^{3+}$  cations in the cathode. This work not only puts forward a novel cathode material for AIBs but also deepens the comprehension on the discharge–charge mechanism which is instructive to design new electrode materials for AIBs.

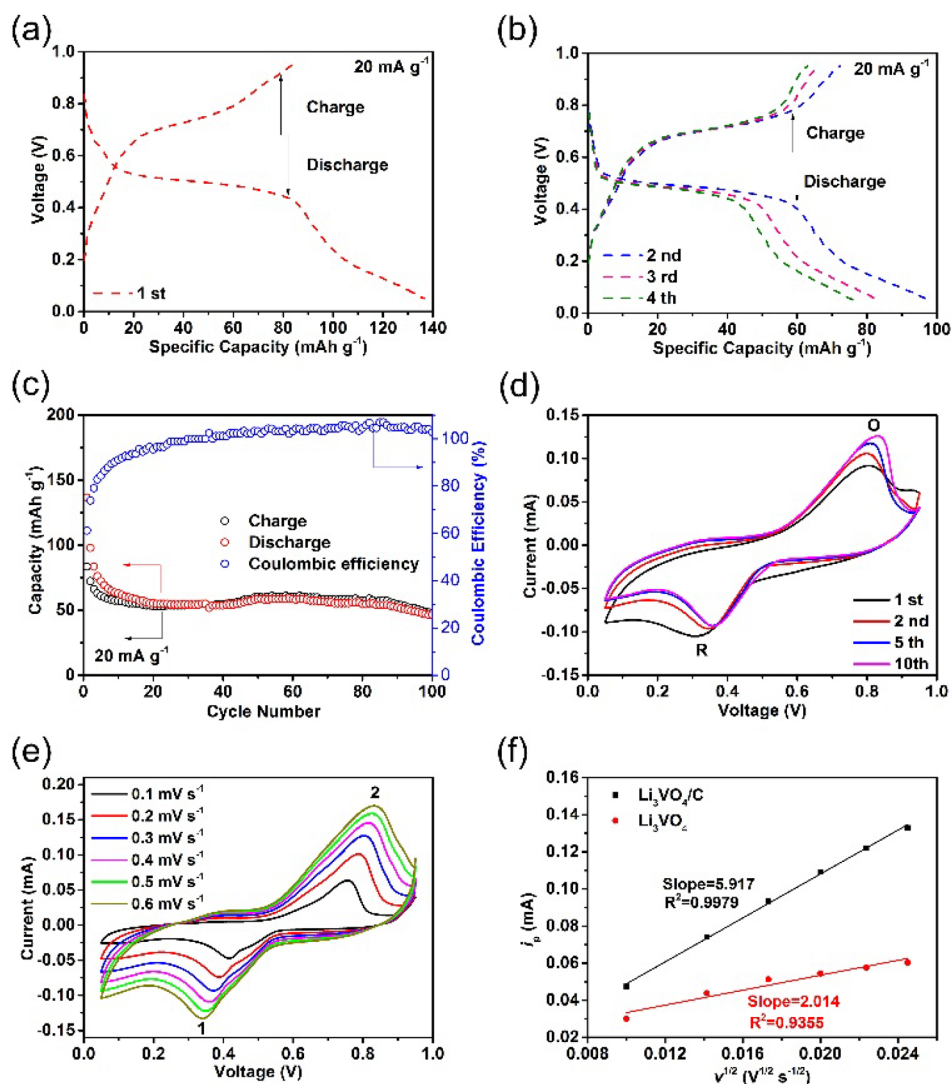


**Figure 2.** Electrochemical characterizations of Al/Li<sub>3</sub>VO<sub>4</sub>@C batteries. (a) Initial discharge/charge curves at a current density of 20 mA g<sup>-1</sup>. (b) Galvanostatic discharge–charge profiles at a current density of 20 mA g<sup>-1</sup> from the second to the fourth cycle. (c) Cycle performance with Coulombic efficiency at a current density of 20 mA g<sup>-1</sup>. All capacity calculations are based on the mass of Li<sub>3</sub>VO<sub>4</sub>@C. The mass of the active materials mainly ranges from 2.0 to 2.5 mg, and the area of electrodes is 1 cm<sup>2</sup>. (d) Cyclic voltammogram (CV) of Li<sub>3</sub>VO<sub>4</sub>@C composite at the scan rate of 0.1 mV s<sup>-1</sup>. (e) CV curves of Li<sub>3</sub>VO<sub>4</sub>@C composite at different scan rates ranging from 0.1 to 0.6 mVs<sup>-1</sup>. (f) Fitted lines of  $i_p$  and  $v^{1/2}$  of reduction peak 1.

## RESULTS AND DISCUSSION

The sample composition and crystal structure of as-synthesized Li<sub>3</sub>VO<sub>4</sub> and Li<sub>3</sub>VO<sub>4</sub>@C were measured by XRD, and the obtained patterns are given in Figure 1a. The diffraction lines of both samples perfectly match with the orthorhombic Li<sub>3</sub>VO<sub>4</sub> (space group: *Pnm*21) with lattice parameters  $a = 5.45 \text{ \AA}$ ,  $b = 6.33 \text{ \AA}$ ,  $c = 4.95 \text{ \AA}$  and  $V = 170.54 \text{ \AA}^3$  (Powder Diffraction File (PDF) No. 38–1247, Joint Committee on Powder Diffraction Standards (JCPDS), 2004). No apparent impure diffraction lines can be observed from the XRD patterns, and the carbon layer coated on the Li<sub>3</sub>VO<sub>4</sub> particles is likely to be amorphous since no diffraction peaks ascribed to crystalline carbon can be found in the XRD patterns. Figure 1b shows the Raman spectra of as-prepared samples. The peaks located from 200 to 500 cm<sup>-1</sup> and from 760 to 950 cm<sup>-1</sup> can be ascribed to the vibration of the Li<sub>3</sub>VO<sub>4</sub> crystal lattice. Two broad peaks near 1358 and 1600 cm<sup>-1</sup> in the Raman spectra of Li<sub>3</sub>VO<sub>4</sub>@C are in accord with the disorder (D-band) and graphite (G-band)

phases of carbon,<sup>23</sup> and there is no vibration peak of Li<sub>3</sub>VO<sub>4</sub> can be detected in Li<sub>3</sub>VO<sub>4</sub>@C sample. The main reason may be that the superficial carbon layer is too thick to be penetrated by a laser wavelength of 532 nm. A laser wavelength of 638 nm or increasing laser intensity can detect the vibration of Li<sub>3</sub>VO<sub>4</sub>, as shown in Figure S4. High-resolution transmission electron microscopy (HR-TEM) of Li<sub>3</sub>VO<sub>4</sub>@C (Figure 1f) can also testify to this assumption.

Field-emission scanning electron microscopy (FESEM) and TEM were performed to obtain the morphology information on synthetic products. Figure S3a,b indicates the SEM images of pristine Li<sub>3</sub>VO<sub>4</sub> particles, which are microspheres ranging from 0.5 to 10 μm in diameter with poriferous and hollow structures. Figure 1c,d are SEM images of Li<sub>3</sub>VO<sub>4</sub>@C composites, and it is easy to see from the smooth surface of spheres that there is a carbon layer coated on the Li<sub>3</sub>VO<sub>4</sub> particles and that the diameters are between 0.5 to 5 μm which means the coated carbon layer can inhibit the growth of spheres. As shown in Figure 1e, the TEM image expressly

reveals the hollow structure of  $\text{Li}_3\text{VO}_4@\text{C}$  microspheres. The selected area electron diffraction (SAED) pattern (the inset of Figure 1e) of the  $\text{Li}_3\text{VO}_4@\text{C}$  particles demonstrates that  $\text{Li}_3\text{VO}_4$  in the composites has a polycrystalline structure as the diffraction spots can be distinctly observed. From the HR-TEM image (Figure 1f) of the  $\text{Li}_3\text{VO}_4@\text{C}$  particle, it can be easily inferred that the thickness of the coated carbon layer is approximately 5 nm, and the carbon layer shows an amorphous and porous structure, which is also deduced by XRD pattern. The lattice fringe spacing of 0.41 nm is consistent with the  $d$ -spacing of (110) plane of orthorhombic  $\text{Li}_3\text{VO}_4$  (PDF No. 38–1247, JCPDS, 2004). According to previous work from our group, the  $\text{Li}_3\text{VO}_4@\text{C}$  composites have a mainly mesoporous structure combined with a narrow pore size distribution of approximately 3.9 nm.<sup>24</sup> Al can get through the porous carbon layer to participate in the insertion/extraction reaction with  $\text{Li}_3\text{VO}_4$ .

To investigate the electrochemical performance of as-prepared samples of AIBs, the galvanostatic discharge/charge measurements were executed in a voltage range of 0.05–0.95 V and at a current density of 20 mA  $\text{g}^{-1}$ . Figure 2a indicates the initial cycle of discharge/charge curves. The initial discharge/charge capacity is 137 and 85 mAh  $\text{g}^{-1}$ , respectively, with the Coulombic efficiency of 62%, which is similar to that of the LIBs (64.5%).<sup>24</sup> Figure 2b shows the discharge/charge curves of the same battery from the second to the fourth cycle. What is the most noteworthy is that the completely overlapped discharge and charge platforms exist at 0.5 and 0.7 V, respectively, which conform to the insertion and extraction of Al in the framework of  $\text{Li}_3\text{VO}_4$ . The discharge/charge capacities for the second cycle are 98 and 74 mAh  $\text{g}^{-1}$  with a Coulombic efficiency of 76%. The irreversible capacity loss can be ascribed to the possibility that  $\text{Al}^{3+}$  ions are trapped in the framework of  $\text{Li}_3\text{VO}_4$  and cannot be extracted to contribute charge capacities, which can be displayed intuitively in the XPS spectra of Al 2p after discharge and charge process (Figure S11). The similar phenomenon is also observed in other metallic oxide systems.<sup>8</sup> In the third and fourth cycles, the discharge capacities are reduced to 84 and 76 mAh  $\text{g}^{-1}$ , respectively. The cycling performance along with corresponding Coulombic efficiency are revealed in Figure 2c at the current density of 20 mA  $\text{g}^{-1}$ , from which it can be illustrated that the capacity decreases relatively slowly, and the electrode indicates a high reversible capacity of over 48 mAh  $\text{g}^{-1}$  after 100 cycles with Coulombic efficiency close to 100%. In short, the  $\text{Li}_3\text{VO}_4@\text{C}$  electrodes exhibit superb structure stability in electrochemical cycling. CV curves of  $\text{Li}_3\text{VO}_4@\text{C}$  and  $\text{Li}_3\text{VO}_4$  electrodes are also performed between 0.05 and 0.95 V at a scan rate of 0.1 mV  $\text{s}^{-1}$  (Figures 2d and S10b) with aluminum foil as counter and reference electrodes. A distinct reduction peak (R) shows at 0.37 V, while an oxidation peak (O) arises around 0.81 V, which is in agreement with the discharge and charge plateaus, indicating that the reaction proceeds in one step, and a pair of current peaks can be assigned to Al reversibly intercalating/deintercalating into one kind of crystallographic sites of  $\text{Li}_3\text{VO}_4$ .<sup>25</sup> The subsequent overlapped curves manifest the excellent electrochemical reversibility of  $\text{Li}_3\text{VO}_4@\text{C}$  electrode in aluminum-ion battery. Figure S10a,b also shows the electrochemical characterizations of pristine  $\text{Li}_3\text{VO}_4$ . The initial discharge/charge capacities at the current density of 20 mA  $\text{g}^{-1}$  are merely 106 and 37 mAh  $\text{g}^{-1}$ , far below the  $\text{Li}_3\text{VO}_4@\text{C}$  electrode. The intensities of the peak current in the CV curves of  $\text{Li}_3\text{VO}_4$  electrode are much weaker, and the potential shifts

of the repeated cycling are much more distinct than that of  $\text{Li}_3\text{VO}_4@\text{C}$  electrode. The results mentioned above may attribute to the structural superiority of  $\text{Li}_3\text{VO}_4@\text{C}$  composite. According to our previous work,<sup>24</sup> the carbon layer covering the spheres can not only promote the electronic conductivity of material but also regulate the size of sphere particles. Furthermore, the geometric structure of mesoporous hollow sphere can enlarge the contact area between electrolyte and active material and reduce the ion diffusion distance. The electrochemical effects of stainless-steel current collector<sup>16,26,27</sup> and polyvinylidene difluoride binder<sup>16,25,28–30</sup> on Al/AlCl<sub>3</sub>-[EMIm]Cl/ $\text{Li}_3\text{VO}_4$  battery system have been elaborated upon in Figures S5–S7.

In order to better research the electrochemical performance of electrode materials, CV analyses of  $\text{Li}_3\text{VO}_4@\text{C}$  and  $\text{Li}_3\text{VO}_4$  at different scan rates were carried out, as indicated in Figures 2e and S10c, respectively. As the scan rate increases, the reduction peaks slowly shift toward lower potential, while the oxidation peaks shift toward higher potential, suggesting the enlarged polarization of battery which is also common in other battery systems.<sup>31</sup> In Figure 2f,  $\text{Li}_3\text{VO}_4@\text{C}$  electrode manifests the better linear relationship ( $R^2 = 0.9979$ ) between the reduction peak current ( $i_p$ ) and the square root of scan rate ( $\nu^{1/2}$ ), and Figure S8 demonstrates the linear relationship between  $\log(i_p)$  and  $\log(\nu)$  plots at different redox states, the obtained  $b$  values of peak 1 (reduction) and peak 2 (oxidation) are 0.5752 and 0.5479, respectively, approximately 0.5, which illustrates the electrochemical reactions in discharge/charge process are mainly ionic diffusion controlled.<sup>32,33</sup> Therefore, the apparent ion diffusion coefficient can be approximately calculated on the basis of the Randles–Sevcik equation:

$$i_p = 0.4463nFAC \left( \frac{nF\nu D}{RT} \right)^{1/2} \quad (1)$$

where  $n$  equals the number of electrons transferred in the redox reaction which usually equals 3 in aluminum-ion batteries,  $F$  is Faraday constant (96 485 C  $\text{mol}^{-1}$ ),  $A$  is the effective surface area between the active material and the electrolyte (1  $\text{cm}^2$ ),  $C$  stands for  $\text{Al}^{3+}$  concentration in the electrode ( $3.053 \times 10^{-3}$  mol  $\text{cm}^{-3}$ ),  $\nu$  is the scan rate,  $R$  is the gas constant (8.314 J  $\text{K}^{-1}$  mol<sup>-1</sup>), and  $T$  is the Kelvin temperature.<sup>23,34,35</sup> According to the slope of  $i_p-\nu^{1/2}$  plots, the apparent diffusion coefficient of reduction peak 1 is calculated to be  $1.928 \times 10^{-12}$   $\text{cm}^2 \text{s}^{-1}$ , which is approximately 8.6-fold that of  $\text{Li}_3\text{VO}_4$  ( $2.233 \times 10^{-13}$   $\text{cm}^2 \text{s}^{-1}$ ), showing the better electrode kinetics of  $\text{Li}_3\text{VO}_4@\text{C}$ . Therefore, it can be concluded that the  $\text{Li}_3\text{VO}_4@\text{C}$  composite improves the aluminum ion diffusion rate, which further accounts for better electrochemical performance of  $\text{Li}_3\text{VO}_4@\text{C}$  electrodes. In addition, galvanostatic intermittent titration technique (GITT) measurement was also carried out to investigate the aluminum ion diffusion coefficients of  $\text{Li}_3\text{VO}_4@\text{C}$  electrode in different discharge states; as demonstrated in Figure S9, the Al-ion diffusion coefficients of  $\text{Li}_3\text{VO}_4@\text{C}$  electrode lie in the range of  $1.198 \times 10^{-12}$ – $5.557 \times 10^{-15}$   $\text{cm}^2 \text{s}^{-1}$ , which is comparable with the apparent diffusion coefficients obtained from CV tests.

Judging from the discharge/charge mechanism of  $\text{Li}_3\text{VO}_4$  in aluminum ion batteries ( $x\text{Al}^{3+} + \text{Li}_3\text{VO}_4 + 3\text{xe}^- \rightarrow \text{Al}_x\text{Li}_3\text{VO}_4$ ), it is notable that the insertion of Al into the framework of  $\text{Li}_3\text{VO}_4$  will be accompanied by the reduction of  $\text{V}^{5+}$ , and the valence state of V in  $\text{Li}_3\text{VO}_4$  can distinctly reflect  $x$  in  $\text{Al}_x\text{Li}_3\text{VO}_4$ . Therefore, XPS spectra of  $\text{Li}_3\text{VO}_4@\text{C}$  electrodes in

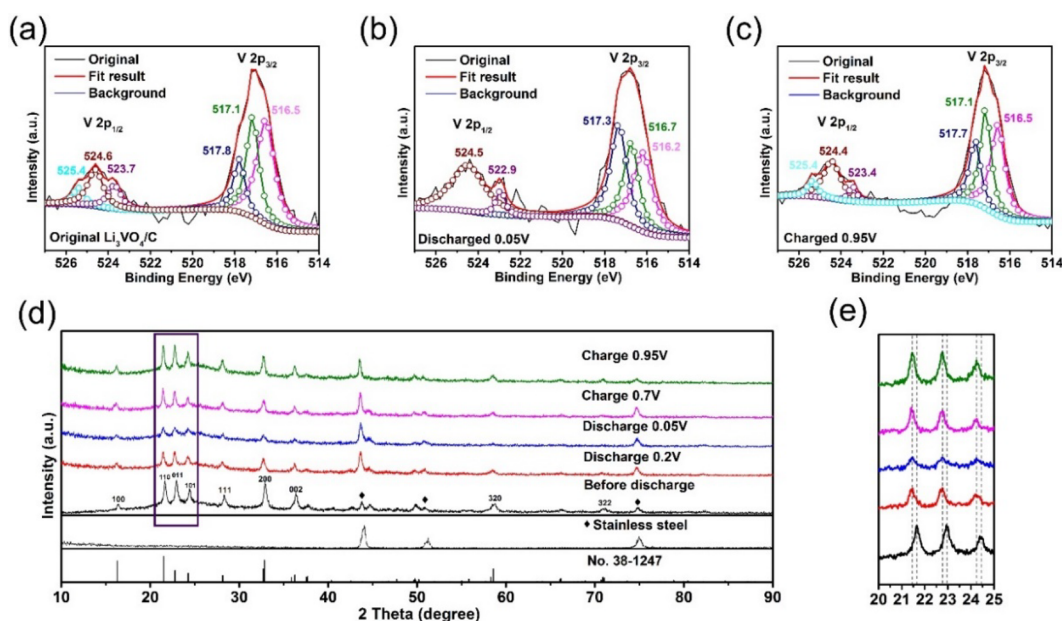


**Figure 3.** (a) V 2p of original  $\text{Li}_3\text{VO}_4@\text{C}$ . (b) V 2p of  $\text{Li}_3\text{VO}_4@\text{C}$  initial discharged to 0.05 V. (c) V 2p of  $\text{Li}_3\text{VO}_4@\text{C}$  initial charged to 0.95 V. (d) Ex situ XRD patterns of the  $\text{Li}_3\text{VO}_4@\text{C}$  electrodes at different insertion/deinsertion depth during the first discharge/charge process. (e) Enlargement of selected region.

different states were characterized to further investigate the electrochemical reaction process. As indicated in Figure 3a, for the fresh  $\text{Li}_3\text{VO}_4@\text{C}$  electrode, three successive peaks near 525.4, 524.6 ( $\text{V}^{5+}$ ), and 523.7 eV ( $\text{V}^{4+}$ ) agree well with V  $2p_{1/2}$ , and another three continuous peaks near 517.8 ( $\text{V}^{4+}$ ), 517.1 ( $\text{V}^{5+}$ ), and 516.5 eV are in correspondence with V  $2p_{3/2}$ .<sup>36–38</sup> The existence of  $\text{V}^{4+}$  may be due to the partial reduction of  $\text{V}^{5+}$  to  $\text{V}^{4+}$  by the carbon source during the heat treatment process.<sup>39</sup> For comparison, the fitted curves of the V 2p spectra for fully discharged and fully charged  $\text{Li}_3\text{VO}_4@\text{C}$  electrodes are indicated in Figure 3b,c, respectively. It is apparent that all the fitted peaks of fully discharged electrode reveal an apparent shift toward the low binding energy region. Simultaneously, the peak area of  $\text{V}^{5+}$  (516.7 eV) decreases, and the peak area of  $\text{V}^{4+}$  (517.3 eV) increases, indicating the reduction of  $\text{V}^{5+}$  to  $\text{V}^{4+}$  in the discharge process. After the  $\text{Li}_3\text{VO}_4@\text{C}$  electrode is initially charged to 0.95 V, all these fitted peaks move toward its original peak positions, and the peak area ratio of  $\text{V}^{5+}$  to  $\text{V}^{4+}$  is close to the original electrode, suggesting the oxidation of  $\text{V}^{4+}$  to  $\text{V}^{5+}$  in the charge process. On the basis of the results discussed above, it may be reasonable to conclude that  $\text{Li}_3\text{VO}_4@\text{C}$  can highly maintain the stability of structure in the intercalation/deintercalation of Al into the framework of  $\text{Li}_3\text{VO}_4$ . Figure S11 displays the XPS spectra of Al 2p in different states, which can visually show that the concentration of Al is augmented with the increasing of discharge depth and reduced with the increase of charge depth, which further indicates that Al can insert/extract reversibly from the materials.

To get further insight into the structural reversibility of  $\text{Li}_3\text{VO}_4@\text{C}$  upon Al intercalation/deintercalation, the ex situ XRD measurements of electrodes at different insertion/deinsertion states were executed, as shown in Figure 3d. It is worth noting that the continuous three diffraction peaks at 21.65, 22.95, and 24.46° match well with the (110), (011), and (101) planes of orthorhombic  $\text{Li}_3\text{VO}_4$  (PDF No. 38–1247, JCPDS, 2004). The peak intensities are slowly reduced with the increasing discharge depth, and the diffraction peaks shift to

slightly lower degrees. It is easy to see from Figure 3e that the displacement distance toward the left is approximately 0.19°, showing the increasing of  $d$  space (about 0.03 Å calculated by Bragg equation), and the crystallinity of electrode materials is decreasing along with the insertion of Al into  $\text{Li}_3\text{VO}_4@\text{C}$ . In the subsequent charge process, the diffraction peak intensities are slowly aggrandizing, but they are slightly lower than that of the original electrode. The  $d$ -spacing distance basically has no change. Figure S12 clearly indicates that the crystallinity of electrode materials decreases and that the displacement distance still retains about 0.2° after 70 cycles. On the basis of the results, it is easy to conclude that the structure of  $\text{Li}_3\text{VO}_4@\text{C}$  will slightly distort irreversibly to accommodate the insertion of  $\text{Al}^{3+}$  in the initial cycle and remain stable in the subsequent cycles. However, such decrease in crystallinity of electrode materials is an accumulation process upon repeated Al intercalation and deintercalation during the discharge/charge cycling. Therefore, the gradual deterioration of crystallinity upon cycling may account for the capacity loss of  $\text{Li}_3\text{VO}_4@\text{C}$  electrode in the subsequent cycles. This phenomenon also occurs in LIBs with  $\text{Li}_3\text{VO}_4$  as anode material.<sup>39</sup>

First-principle calculations are available to further unravel the mechanism how aluminum ion intercalated into the  $\text{Li}_3\text{VO}_4$ .<sup>40–43</sup> As mentioned in CV curves, Al can reversibly intercalate/deintercalate into one kind of crystallographic site of  $\text{Li}_3\text{VO}_4$ , which possesses two possible insertion sites to hold Al (shown in Figure 4a). Corresponding theoretical calculations were performed to elucidate which site is preferred. We optimized structures of  $\text{Al}_x\text{Li}_3\text{VO}_4$  with Al in the a or b site, respectively. The results are shown in Table 1. The calculated lattice parameters of  $\text{Li}_3\text{VO}_4$  fit well with its experimental data,<sup>44</sup> which means the calculation setting and the model are reliable. It is also obvious that the calculated free energy for Al intercalated into the a and b sites are  $-4.35$  and  $-3.22$  eV, respectively, suggesting that Al is more stable in the a site. The changes of all lattice parameters of  $\text{Li}_3\text{VO}_4$ , when Al is inserted into the a site, are almost 0.1 Å as verified by XRD, indicating

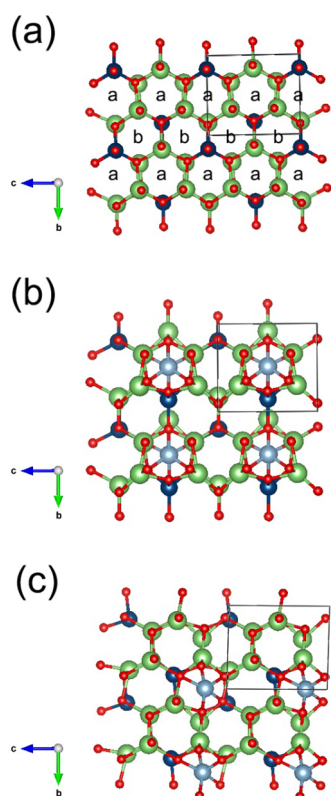


**Figure 4.** View of the optimized crystal structures of  $\text{Al}_x\text{Li}_3\text{VO}_4$  projected along  $a$ -axis. (a) Initial  $\text{Li}_3\text{VO}_4$ , with  $a$  and  $b$  sites to accommodate Al insertion. Ball and stick model of  $\text{Li}_3\text{VO}_4$  with Al inserted into (b)  $a$  site and (c)  $b$  site. Color code: Li, green; V, dark blue; O, red; Al: light blue.

that limited amount of Al inserted into a site does not result in overexpansion of the structure. The main reason may be that the attractive force between Al and O is much stronger than that of Li and O, and inserted Al will attract eight O atoms nearby, causing a certain volume shrinkage. However, the repulsive force between the inserted Al and V/Li will cause volume expansion; ultimately, the volume change is not obvious when a certain amount of Al intercalated into a site. In consideration of the experimental amount of Al inserted into  $\text{Li}_3\text{VO}_4$  being less than  $1/2$  (calculation based on capacities), the optimized model of  $\text{Al}_{1/3}\text{Li}_3\text{VO}_4$  is also shown in Table 1, indicating less structural changes than  $\text{Al}_{1/2}\text{Li}_3\text{VO}_4$ .

The morphology and composition characterizations of  $\text{Li}_3\text{VO}_4@\text{C}$  electrodes before and after electrochemical tests have also been measured to investigate the changes of cathode materials. Figure 5 shows the TEM images and corresponding HRTEM images of the  $\text{Li}_3\text{VO}_4@\text{C}$  cathode materials in different discharge/charge states. It can be observed that the morphology of spheres is still well-maintained upon initial discharge/charge process; of note is that the microsphere

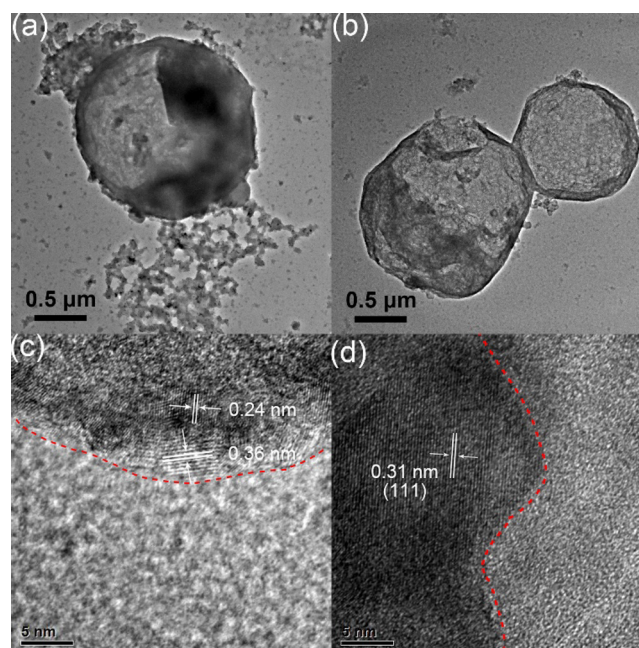


**Figure 5.** TEM and HRTEM images of the  $\text{Li}_3\text{VO}_4@\text{C}$  (a, c) discharged to 0.05 V and (b, d) charged to 0.95 V.

morphology of  $\text{Li}_3\text{VO}_4@\text{C}$  after 100 cycles is also well-maintained (Figure S14), which confirmed the excellent structural stability of  $\text{Li}_3\text{VO}_4@\text{C}$  in long cycling. The relevant HRTEM images after initial discharge and charge are exhibited in Figure 5c,d, and the distinct lattice fringes illustrate that  $\text{Li}_3\text{VO}_4@\text{C}$  still retains crystallinity to a certain extent. Thereinto, the lattice fringe spacing of 0.24 and 0.36 nm in Figure 5c match well with the  $d$ -spacing of (002) plane and (101) plane of the orthorhombic  $\text{Li}_3\text{VO}_4$ , and 0.31 nm in Figure 5d agrees well with the  $d$ -spacing of (111) plane.<sup>9,36</sup> Figure S13 indicates the correlative SAED patterns in different discharge/charge states. The blurry SAED rings in Figure S13d show the crystallinity of material decreases after discharged to 0.05 V, and the SAED ring patterns in Figure S13f can match well with those of (011) and (200) planes,<sup>45</sup> which manifests the reinstatement of crystallinity in the charge process. Energy-dispersive X-ray spectroscopy (EDS) of the electrode after initial discharge process displayed in Figure S13g distinctly reveals the presence of C, V, O, and Al elements. Figure 6 exhibits the corresponding EDS mapping of  $\text{Li}_3\text{VO}_4@\text{C}$  electrode after discharged to 0.05 V, the C, O, V, and Al elements coexist and evenly distribute in the spheres.

To further explore the electrochemical reaction process taking place in Al/ $\text{Li}_3\text{VO}_4@\text{C}$  battery system,<sup>27</sup>Al NMR spectra of the  $\text{AlCl}_3/[\text{EMIm}]\text{Cl}$  ionic liquid electrolytes in different states were obtained to investigate the ionic compositions and the corresponding contents in discharge/charge process. As shown in Figure 7, one broad peak at 103.95

**Table 1.** Lattice Parameters for  $\text{Li}_3\text{VO}_4$  (Experimental and Calculated) and  $\text{Al}_x\text{Li}_3\text{VO}_4$

structure	$a, b, c$ (Å)	$\alpha, \beta, \gamma$ (deg)	$\Delta G$ (eV)
$\text{Li}_3\text{VO}_4$ <sup>44</sup>	6.3259(12), 5.4460(8), 4.9460(9)	90.0, 90.0, 90.0	
$\text{Li}_3\text{VO}_4$	6.38289, 5.50061, 5.03147	90.0, 90.0, 90.0	
$\text{Li}_3\text{Al}_{1/2}\text{VO}_4$ (a)	6.22159, 5.51365, 5.07447	91.4, 90.0, 90.0	-4.35
$\text{Li}_3\text{Al}_{1/2}\text{VO}_4$ (b)	6.61605, 5.50503, 5.07852	89.9, 87.2, 88.7	-3.22
$\text{Li}_3\text{Al}_{1/3}\text{VO}_4$ (a)	6.21805, 5.55101, 5.11558	90.4, 90.0, 90.0	-4.09

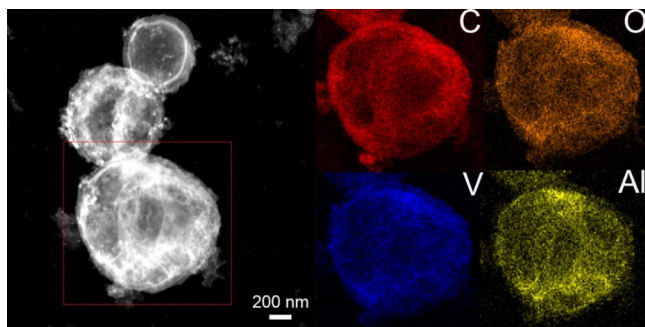


**Figure 6.** High-angle annular dark field (HAADF) images of  $\text{Li}_3\text{VO}_4@\text{C}$  discharged to 0.05 V and corresponding EDS mapping images of C, O, V, and Al elements in the selected region.

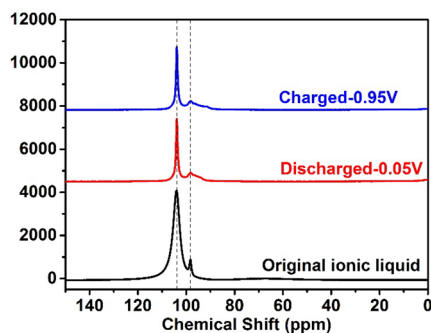


**Figure 7.**  $^{27}\text{Al}$  NMR spectra of the  $\text{AlCl}_3/[\text{EMIm}]\text{Cl}$  ionic liquid electrolyte with a molar ratio of 1.3 in different states.

ppm and the comparatively small peak at 98.15 ppm for the electrolyte of  $\text{AlCl}_3/[\text{EMIm}]\text{Cl} = 1.3:1$  can be assigned to  $\text{AlCl}_4^-$  and  $\text{Al}_2\text{Cl}_7^-$ , respectively,<sup>46</sup> showing that both  $\text{AlCl}_4^-$  and  $\text{Al}_2\text{Cl}_7^-$  are major anions in the acidic ionic liquid electrolyte before and after electrochemical tests. The ratio of  $\text{AlCl}_4^-$  to  $\text{Al}_2\text{Cl}_7^-$  is calculated as approximately 6.98:1 in the original ionic liquid, but the ratio decreases to nearly 3.61:1 after initial discharge which reflects the  $\text{AlCl}_4^-$  anions in electrolyte reacting with  $\text{Al}^{3+}$  to form larger  $\text{Al}_2\text{Cl}_7^-$  anions. Also, the ratio of  $\text{AlCl}_4^-$  to  $\text{Al}_2\text{Cl}_7^-$  in electrolyte increases to 5.45:1 as charged to 0.95 V, which represents the reverse reaction process.<sup>9,13,30</sup>

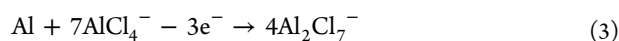
As described above, the discharge/charge reaction process of the  $\text{Al}/\text{AlCl}_3\text{-}[\text{EMIm}]\text{Cl}/\text{Li}_3\text{VO}_4@\text{C}$  battery system can be formulated as the following equations:

In the discharge process:

Cathode:

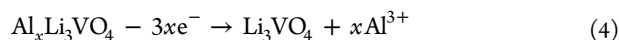


Anode:



In the charge process:

Cathode:



Anode:



Hence, the schematic illustration of the aluminum-ion battery during the discharge process is revealed in **Figure 8**.

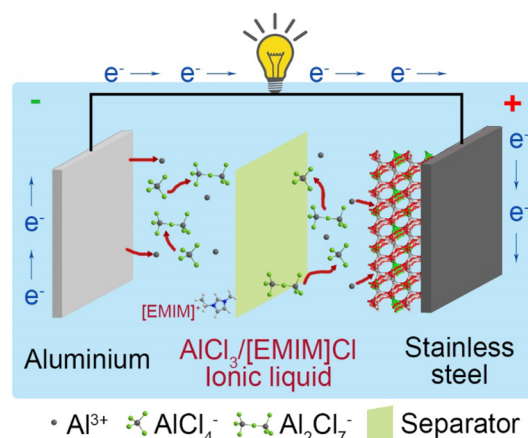


**Figure 8.** Schematic illustration of the  $\text{Al}/\text{AlCl}_3\text{-}[\text{EMIm}]\text{Cl}/\text{Li}_3\text{VO}_4@\text{C}$  battery during the discharge process, using the optimal proportion of the  $\text{AlCl}_3/[\text{EMIm}]\text{Cl}$  ionic liquid electrolyte. On the cathode side, predominantly  $\text{Al}^{3+}$  cations intercalate and deintercalate in the tunnel structure of  $\text{Li}_3\text{VO}_4@\text{C}$  during discharge and charge process, respectively. On the anode side,  $\text{Al}_2\text{Cl}_7^-$  is produced by the reaction of metallic Al with  $\text{AlCl}_4^-$  during discharging, and the reverse reaction occurs during charging.

On the cathode side, principally  $\text{Al}^{3+}$  cations insert and deinsert in the tunnel structure of  $\text{Li}_3\text{VO}_4@\text{C}$  during the discharge and charge processes, respectively. On the anode side,  $\text{Al}_2\text{Cl}_7^-$  is produced by the reaction of metallic Al with  $\text{AlCl}_4^-$  during discharging, and the reverse reaction occurs during charging. It can be deduced that  $\text{Al}_2\text{Cl}_7^-$  is the electrochemically active ion in electrolyte, which is present as the molar ratio of  $\text{AlCl}_3$  to  $[\text{EMIm}]\text{Cl}$  is greater than 1.1:1 (**Figure S1**). Combined with the results obtained from **Figures S1 and S2**, the optimal proportion of the  $\text{AlCl}_3/[\text{EMIm}]\text{Cl}$  ionic liquid, namely, the ratio of 1.3, is used as the AIBs electrolyte in this work.

**Figure S15** shows the appearance changes of positive and negative electrodes before and after electrochemical test. It can be readily observed from the  $\text{Li}_3\text{VO}_4@\text{C}$  electrode that there is basically no change in the surface (**Figure S15c**) and no volume expansion with the naked eyes (**Figure S15b**). Nevertheless, the surface of Al anode blackens after 100 cycles (**Figure S15a**). To enrich the in-depth understanding of the black substance, the XRD pattern of Al anode after 100 cycles was obtained (**Figure S16**). The diffraction peaks of Al anode have no change before and after electrochemical cycling, which indicates that aluminum ions deposit back to the surface of Al anode in the form of nanoparticles.

## CONCLUSIONS

$\text{Li}_3\text{VO}_4@\text{C}$  microspheres composite exhibits the ability to insert Al reversibly with acidic ionic liquid as electrolyte. The initial discharge capacity of  $\text{Al}/\text{Li}_3\text{VO}_4@\text{C}$  battery is  $137 \text{ mAh g}^{-1}$  and remains at  $48 \text{ mAh g}^{-1}$  after 100 cycles with the Coulombic efficiency close to 100% at the current density of  $20 \text{ mA g}^{-1}$ . Furthermore, the detailed intercalation mechanism of Al into the orthorhombic  $\text{Li}_3\text{VO}_4$  was characterized by ex situ XRD and XPS spectra of  $\text{Li}_3\text{VO}_4@\text{C}$  electrodes and the  $^{27}\text{Al}$  NMR spectra of ionic liquid electrolyte in different states. It is easy to conclude that the structure of  $\text{Li}_3\text{VO}_4@\text{C}$  will slightly distort irreversibly to accommodate the insertion of Al in the initial cycle and remain stable in the subsequent cycles. The first-principle calculations also elucidate Al mainly inserts into a site

of  $\text{Li}_3\text{VO}_4$ , and there are scarcely any structural changes after intercalation. Even though the battery system in this work suffers from low capacity and low discharge plateau, such rechargeable AIBs are low-cost, safe, and still may make a step forward in the development of novel cathode materials based on acidic ionic liquid electrolyte system.

## EXPERIMENTAL SECTION

**Preparation of Composite.** The mesoporous  $\text{Li}_3\text{VO}_4@\text{C}$  hollow spheres were prepared by a spray-drying process and subsequent heat treatment in argon atmosphere. In a typical synthesis, 6 mmol of  $\text{Li}_2\text{CO}_3$  (0.444 g), 2 mmol of  $\text{V}_2\text{O}_5$  (0.364 g), and 0.9 g of glucose were added into 70 mL of distilled water. After magnetic stirring for several hours, the generated clear solution was spray-dried by a Buchi mini spray B-290 at the inlet temperature of 205 °C, with aspirator rate of 100%, rotameter setting of 40 mm, and sampling pump rate of 10% (3.0 mL/min). Nitrogen was used as the carrier gas. The precursors were annealed at 550 °C for 5 h in argon atmosphere;  $\text{Li}_3\text{VO}_4@\text{C}$  hollow spheres were obtained. The pristine  $\text{Li}_3\text{VO}_4$  was synthesized by a similar method in the absence of glucose.

**Synthesis of Ionic Liquid Electrolytes.** The ionic liquid electrolytes ( $[\text{EMImAl}_x\text{Cl}_y]$ ) were prepared by slowly dissolving anhydrous aluminum chloride ( $\text{AlCl}_3$ , 99%, Aladdin) in heat-treated 1-ethyl-3-methylimidazolium chloride ( $[\text{EMIm}]\text{Cl}$ , 98%, Aladdin). The obtained transparent light-yellow liquid was magnetically stirred at room temperature for several minutes, followed by standing for at least 12 h. The whole preparation process was operated under an argon-atmosphere glovebox (M. Braun, Germany). The molar ratio of  $\text{AlCl}_3$  to  $[\text{EMIm}]\text{Cl}$  varied from 0.8 to 1.5. The  $^{27}\text{Al}$  NMR spectra of room-temperature ionic liquids were recorded on the Bruker Avance II 400 spectrometer with 1.0 M  $\text{Al}(\text{NO}_3)_3$  aqueous solution as the external chemical shift standard. In addition, as-synthesized ionic liquids were characterized by Fourier transform infrared spectrometer (Nicolet iS5). Cyclic voltammetry (CV) was measured by soft package battery on the CHI1030C potentiostat (Shanghai Chenhua Instruments, PR China) at a scan rate of 0.1 mV/s. Al foil was used as the counter and reference electrodes, while Au foil was used as the working electrode. Al electrode was treated by polishing with fine sand paper, followed by rinsing in ionic liquid electrolyte for 5 min to remove the oxide layer on the surface of metallic aluminum.

**Electrochemical Measurements.** The electrochemical properties of the as-prepared mesoporous  $\text{Li}_3\text{VO}_4@\text{C}$  hollow spheres were measured in 1 cm × 1 cm soft package battery with metallic aluminum as anode material. The cathode material was a slurry consisted of 70 wt % active material ( $\text{Li}_3\text{VO}_4@\text{C}$ , ~100 mg), 20 wt % acetylene black, and 10 wt % polyvinylidene difluoride binder in *N*-methyl-2-pyrrolidinone (NMP). The slurry was coated on the stainless-steel mesh and dried in vacuum oven at 60 °C overnight to remove residual NMP. The loading of active materials on the electrodes is around 2.0–2.5 mg/cm<sup>2</sup>. The electrolyte used for aluminum-ion battery was the mixture of anhydrous  $\text{AlCl}_3$  and  $[\text{EMIm}]\text{Cl}$  with 1.3:1 mol ratio. All cells were fabricated in an argon-filled glovebox (M. Braun, Germany). The galvanostatic charge–discharge measurements and GITT test were executed on the Neware CT-3008W battery test system (Neware Battery Testing Instruments, PR China). The CV measurements were conducted on a CHI 1030C potentiostat.

**Characterization.** The X-ray diffraction (XRD) patterns were obtained by Rigaku Miniflex 600 (Rigaku Corporation, Japan) with  $\text{Cu K}\alpha$  radiation source operated at 40 kV, 15 mA. The scanning rate is 2° min<sup>-1</sup>, and the scanning range is 10–90° (2 theta). The Raman spectra were obtained using a Renishaw spectrophotometer (Renishaw plc., UK). The morphology of the original materials was analyzed on the Hitachi S-4800 and Hitachi TM-3030 (Hitachi Corporation, Japan) by SEM and TEM, and SAED patterns were recorded on the JEM-2100 (JEOL, Japan) at 200 kV. HR-TEM and EDS linear sweep tests were operated on Tecnai F30 (FEI, US) at the accelerating voltage of 300 kV. XPS was tested with PHI Quantum 2000 scanning ESCA microprobe with Al  $\text{K}\alpha$  radiation (1486.6 eV) (Physical Electronics, Inc. USA).

**Computations.** Structure optimization of  $\text{Li}_3\text{VO}_4$ ,  $\text{Al}_{1/2}\text{Li}_3\text{VO}_4$ , and Al were performed by Vienna Ab-initio Simulation Package (VASP). We opted the projector augmented wave pseudopotential with GGA+U framework and chose the PBE form for the exchange-correction functional. The energy cutoff value was 520 eV for all performed calculations, and the spins polarized were considered in all calculations. For DFT+U calculations, we followed the simplified approach to the LSDA+U. The U value was set to 2 eV for V, and J was fixed to 0 eV. The tendencies of Al insertion of different sites were estimated by the following equations, in which G was the free energy of the given structure:

$$\Delta G = G(\text{Li}_3\text{Al}_{1/2}\text{VO}_4) - G(\text{Li}_3\text{VO}_4) - 1/2 G(\text{Al})$$

$$\Delta G = G(\text{Li}_3\text{Al}_{1/3}\text{VO}_4) - G(\text{Li}_3\text{VO}_4) - 1/3 G(\text{Al})$$

## ASSOCIATED CONTENT

### Supporting Information

The Supporting Information is available free of charge on the ACS Publications website at DOI: 10.1021/acsami.7b07503.

Electrochemical and physical characterization of ionic liquid, electrochemical performance of  $\text{Li}_3\text{VO}_4$ , detailed calculations of ion diffusion coefficients from CV tests and GITT test, and electrochemical characterization of stainless steel and PVDF (PDF)

## AUTHOR INFORMATION

### Corresponding Author

\*E-mail: jbzhaoy@xmu.edu.cn.

### ORCID

He Li: 0000-0002-5324-8101

Jinbao Zhao: 0000-0002-2753-7508

### Notes

The authors declare no competing financial interest.

## ACKNOWLEDGMENTS

This work was financially supported by National Natural Science Foundation of China (Nos. 21321062 and 21603179) and the Fundamental Research Funds for the Central Universities (No. 20720170021). We thank Prof. Daiwei Liao of Xiamen University for his valuable suggestions on this work.

## REFERENCES

- (1) Stephenson, T.; Li, Z.; Olsen, B.; Mitlin, D. Lithium Ion Battery Applications of Molybdenum Disulfide ( $\text{MoS}_2$ ) Nanocomposites. *Energy Environ. Sci.* **2014**, *7*, 209–231.
- (2) Slater, M. D.; Kim, D.; Lee, E.; Johnson, C. S. Sodium-Ion Batteries. *Adv. Funct. Mater.* **2013**, *23*, 947–958.
- (3) Hu, Z.; Zhu, Z.; Cheng, F.; Zhang, K.; Wang, J.; Chen, C.; Chen, J. Pyrite  $\text{FeS}_2$  for High-rate and Long-life Rechargeable Sodium Batteries. *Energy Environ. Sci.* **2015**, *8*, 1309–1316.
- (4) Shi, C.; Li, X.; He, X.; Zhao, J. New Insight into the Interaction between Carbonate-based Electrolyte and Cuprous Sulfide Electrode Material for Lithium Ion Batteries. *Electrochim. Acta* **2015**, *174*, 1079–1087.
- (5) Wang, Y.; Li, X.; Zhang, Y.; He, X.; Zhao, J. Ether Based Electrolyte Improves the Performance of  $\text{CuFeS}_2$  Spike-like Nanorods as a Novel Anode for Lithium Storage. *Electrochim. Acta* **2015**, *158*, 368–373.
- (6) Sun, H.; Wang, W.; Yu, Z.; Yuan, Y.; Wang, S.; Jiao, S. A New Aluminium-ion Battery with High Voltage, High Safety and Low Cost. *Chem. Commun.* **2015**, *51*, 11892–11895.
- (7) Tong, X.; Zhang, F.; Ji, B.; Sheng, M.; Tang, Y. Carbon-Coated Porous Aluminum Foil Anode for High-Rate, Long-Term Cycling

Stability, and High Energy Density Dual-Ion Batteries. *Adv. Mater.* **2016**, *28*, 9979–9985.

(8) Wang, H.; Bai, Y.; Chen, S.; Luo, X.; Wu, C.; Wu, F.; Lu, J.; Amine, K. Binder-free  $V_2O_5$  Cathode for Greener Rechargeable Aluminum Battery. *ACS Appl. Mater. Interfaces* **2015**, *7*, 80–84.

(9) Liang, Z.; Lin, Z.; Zhao, Y.; Dong, Y.; Kuang, Q.; Lin, X.; Liu, X.; Yan, D. New Understanding of  $Li_3VO_4/C$  as Potential Anode for Li-ion Batteries: Preparation, Structure Characterization and Lithium Insertion Mechanism. *J. Power Sources* **2015**, *274*, 345–354.

(10) Wang, H.; Gu, S.; Bai, Y.; Chen, S.; Zhu, N.; Wu, C.; Wu, F. Anion-effects on Electrochemical Properties of Ionic Liquid Electrolytes for Rechargeable Aluminum Batteries. *J. Mater. Chem. A* **2015**, *3*, 22677–22686.

(11) Ambroz, F.; Macdonald, T. J.; Nann, T. Trends in Aluminium-Based Intercalation Batteries. *Adv. Energy Mater.* **2017**, 1602093.

(12) Mori, T.; Orikasa, Y.; Nakanishi, K.; Kezheng, C.; Hattori, M.; Ohta, T.; Uchimoto, Y. Discharge/Charge Reaction Mechanisms of  $FeS_2$  Cathode Material for Aluminum Rechargeable Batteries at 55°C. *J. Power Sources* **2016**, *313*, 9–14.

(13) Wang, S.; Yu, Z.; Tu, J.; Wang, J.; Tian, D.; Liu, Y.; Jiao, S. A Novel Aluminum-Ion Battery:  $Al/AlCl_3-[EMIm]Cl/Ni_3S_2@Graphene$ . *Adv. Energy Mater.* **2016**, *6*, 1600137.

(14) Yang, G. Y.; Chen, L.; Jiang, P.; Guo, Z. Y.; Wang, W.; Liu, Z. P. Fabrication of Tunable 3D Graphene Mesh Network with Enhanced Electrical and Thermal Properties for High-rate Aluminum-ion Battery Application. *RSC Adv.* **2016**, *6*, 47655–47660.

(15) Yu, X.; Wang, B.; Gong, D.; Xu, Z.; Lu, B. Graphene Nanoribbons on Highly Porous 3D Graphene for High-Capacity and Ultra-stable Al-Ion Batteries. *Adv. Mater.* **2017**, *29*, 1604118.

(16) Geng, L.; Lv, G.; Xing, X.; Guo, J. Reversible Electrochemical Intercalation of Aluminum in  $Mo_6S_8$ . *Chem. Mater.* **2015**, *27*, 4926–4929.

(17) Liu, S.; Pan, G. L.; Li, G. R.; Gao, X. P. Copper Hexacyanoferrate Nanoparticles as Cathode Material for Aqueous Al-ion Batteries. *J. Mater. Chem. A* **2015**, *3*, 959–962.

(18) Reed, L. D.; Ortiz, S. N.; Xiong, M.; Menke, E. J. A Rechargeable Aluminum-ion Battery Utilizing a Copper Hexacyanoferrate Cathode in an Organic Electrolyte. *Chem. Commun.* **2015**, *51*, 14397–14400.

(19) Stadie, N. P.; Wang, S.; Kravchuk, K. V.; Kovalenko, M. V. Zeolite-Templated Carbon as an Ordered Microporous Electrode for Aluminum Batteries. *ACS Nano* **2017**, *11*, 1911–1919.

(20) Elia, G. A.; Marquardt, K.; Hoeppe, K.; Fantini, S.; Lin, R.; Knipping, E.; Peters, W.; Drillet, J. F.; Passerini, S.; Hahn, R. An Overview and Future Perspectives of Aluminum Batteries. *Adv. Mater.* **2016**, *28*, 7564–7579.

(21) Li, H.; Liu, X.; Zhai, T.; Li, D.; Zhou, H.  $Li_3VO_4$ : A Promising Insertion Anode Material for Lithium-Ion Batteries. *Adv. Energy Mater.* **2013**, *3*, 428–432.

(22) Ni, S.; Lv, X.; Ma, J.; Yang, X.; Zhang, L. Electrochemical Characteristics of Lithium Vanadate,  $Li_3VO_4$  as a New Sort of Anode Material for Li-ion Batteries. *J. Power Sources* **2014**, *248*, 122–129.

(23) Zhang, C.; Song, H.; Liu, C.; Liu, Y.; Zhang, C.; Nan, X.; Cao, G. Fast and Reversible Li Ion Insertion in Carbon-Encapsulated  $Li_3VO_4$  as Anode for Lithium-Ion Battery. *Adv. Funct. Mater.* **2015**, *25*, 3497–3504.

(24) Yang, Y.; Li, J.; He, X.; Wang, J.; Sun, D.; Zhao, J. A Facile Spray Drying Route for Mesoporous  $Li_3VO_4/C$  Hollow Spheres as an Anode for Long Life Lithium Ion Batteries. *J. Mater. Chem. A* **2016**, *4*, 7165–7168.

(25) Lee, B.; Lee, H. R.; Yim, T.; Kim, J. H.; Lee, J. G.; Chung, K. Y.; Cho, B. W.; Oh, S. H. Investigation on the Structural Evolutions during the Insertion of Aluminum Ions into  $Mo_6S_8$  Chevrel Phase. *J. Electrochem. Soc.* **2016**, *163*, A1070–A1076.

(26) Geng, L.; Scheifers, J. P.; Fu, C.; Zhang, J.; Fokwa, B. P. T.; Guo, J. Titanium Sulfides as Intercalation-Type Cathode Materials for Rechargeable Aluminum Batteries. *ACS Appl. Mater. Interfaces* **2017**, *9*, 21251–21257.

(27) Wang, H.; Bi, X.; Bai, Y.; Wu, C.; Gu, S.; Chen, S.; Wu, F.; Amine, K.; Lu, J. Open-Structured  $V_2O_5 \cdot nH_2O$  Nanoflakes as Highly Reversible Cathode Material for Monovalent and Multivalent Intercalation Batteries. *Adv. Energy Mater.* **2017**, *7*, 1602720.

(28) Cohn, G.; Ma, L.; Archer, L. A. A Novel Non-Aqueous Aluminum Sulfur Battery. *J. Power Sources* **2015**, *283*, 416–422.

(29) Zhang, L.; Chen, L.; Luo, H.; Zhou, X.; Liu, Z. Large-Sized Few-Layer Graphene Enables an Ultrafast and Long-Life Aluminum-Ion Battery. *Adv. Energy Mater.* **2017**, 1700034.

(30) Wang, S.; Jiao, S.; Wang, J.; Chen, H. S.; Tian, D.; Lei, H.; Fang, D. N. High-Performance Aluminum-Ion Battery with  $CuS@C$  Microsphere Composite Cathode. *ACS Nano* **2017**, *11*, 469–477.

(31) Li, H.; Wang, Y.; Huang, J.; Zhang, Y.; Zhao, J. Microwave-assisted Synthesis of  $CuS/Graphene$  Composite for Enhanced Lithium Storage Properties. *Electrochim. Acta* **2017**, *225*, 443–451.

(32) Zhang, K.; Hu, Z.; Liu, X.; Tao, Z.; Chen, J.  $FeSe_2$  Microspheres as a High-Performance Anode Material for Na-Ion Batteries. *Adv. Mater.* **2015**, *27*, 3305–3309.

(33) Li, H.; Jiang, J.; Wang, F.; Huang, J.; Wang, Y.; Zhang, Y.; Zhao, J. Facile Synthesis of Rod-like  $Cu_{2-x}Se$  and Insight into its Improved Lithium-Storage Property. *ChemSusChem* **2017**, *10*, 2235–2241.

(34) Yang, Y.; Qiao, B.; Yang, X.; Fang, L.; Pan, C.; Song, W.; Hou, H.; Ji, X. Lithium Titanate Tailored by Cathodically Induced Graphene for an Ultrafast Lithium Ion Battery. *Adv. Funct. Mater.* **2014**, *24*, 4349–4356.

(35) Kim, H.; Lee, J.; Ahn, H.; Kim, O.; Park, M. J. Synthesis of Three-Dimensionally Interconnected Sulfur-rich Polymers for Cathode Materials of High-rate Lithium-sulfur Batteries. *Nat. Commun.* **2015**, *6*, 7278.

(36) Ni, S.; Zhang, J.; Ma, J.; Yang, X.; Zhang, L.; Li, X.; Zeng, H. Approaching the Theoretical Capacity of  $Li_3VO_4$  via Electrochemical Reconstruction. *Adv. Mater. Interfaces* **2016**, *3*, 1500340.

(37) Silversmit, G.; Depla, D.; Poelman, H.; Marin, G. B.; De Gryse, R. Determination of the V2p XPS Binding Energies for Different Vanadium Oxidation States ( $V^{5+}$  to  $V^{0+}$ ). *J. Electron Spectrosc. Relat. Phenom.* **2004**, *135*, 167–175.

(38) Gu, S.; Wang, H.; Wu, C.; Bai, Y.; Li, H.; Wu, F. Confirming Reversible  $Al^{3+}$  Storage Mechanism Through Intercalation of  $Al^{3+}$  into  $V_2O_5$  Nanowires in a Rechargeable Aluminum Battery. *Energy Storage Mater.* **2017**, *6*, 9–17.

(39) Liao, C.; Wen, Y.; Shan, B.; Zhai, T.; Li, H. Probing the Capacity Loss of  $Li_3VO_4$  Anode Upon Li Insertion and Extraction. *J. Power Sources* **2017**, *348*, 48–56.

(40) Kresse, G.; Furthmüller, J. Efficient Iterative schemes for ab Initio Total-energy Calculations using a Plane-wave Basis Set. *Phys. Rev. B: Condens. Matter Mater. Phys.* **1996**, *54*, 11169–11186.

(41) Blöchl, P. E. Projector Augmented-wave Method. *Phys. Rev. B: Condens. Matter Mater. Phys.* **1994**, *50*, 17953–17979.

(42) Perdew, J. P.; Burke, K.; Ernzerhof, M. Generalized Gradient Approximation Made Simple. *Phys. Rev. Lett.* **1996**, *77*, 3865–3868.

(43) Dudarev, S.; Botton, G.; Savrasov, S. Y.; Szotek, Z.; Temmerman, W.; Sutton, A. Electronic Structure and Elastic Properties of Strongly Correlated Metal Oxides from First Principles: LSDA + U, SIC-LSDA and EELS Study of  $UO_2$  and  $NiO$ . *Phys. Status Solidi A* **1998**, *166*, 429–443.

(44) Shannon, R. D.; Calvo, C. Refinement of the Crystal Structure of Low Temperature  $Li_3VO_4$  and Analysis of Mean bond Lengths in Phosphates, Arsenates, and Vanadates. *J. Solid State Chem.* **1973**, *6*, 538–549.

(45) Kim, W.-T.; Min, B.-K.; Choi, H. C.; Lee, Y. J.; Jeong, Y. U. Lithium Intercalation and Crystal Chemistry of  $Li_3VO_4$  Synthesized by Ultrasonic Nebulization as a New Anode Material for Secondary Lithium Batteries. *J. Electrochem. Soc.* **2014**, *161*, A1302–A1305.

(46) Sun, X. G.; Fang, Y.; Jiang, X.; Yoshii, K.; Tsuda, T.; Dai, S. Polymer Gel Electrolytes for Application in Aluminum Deposition and Rechargeable Aluminum Ion Batteries. *Chem. Commun.* **2016**, *52*, 292–295.